

Magnetic criticality and magnetocaloric response in MnBi_2Te_4 and MnBi_4Te_7

Nazma Firdosh¹, Shreyashi Sinha¹ and Sujit Manna^{1*}

¹*Department of Physics, Indian Institute of Technology Delhi, Hauz Khas, New Delhi 110016, India*

(Dated: March 12, 2026)

MnBi_2Te_4 and MnBi_4Te_7 are antiferromagnetic topological insulators belonging to the $\text{MnBi}_{2n}\text{Te}_{3n+1}$ series, where structural layering provides a natural route to tune magnetic interaction in van der Waals magnets. Despite extensive interest in their topological properties, how the insertion of Bi_2Te_3 quintuple layers modifies magnetic critical fluctuations near the antiferromagnetic transition remains unresolved. Here, we combine scanning tunneling microscopy (STM), critical scaling analysis, and magnetocaloric measurements to directly correlate real-space structures with magnetic criticality. STM reveals atomically flat septuple-layer terraces in MnBi_2Te_4 whereas MnBi_4Te_7 displays coexisting septuple and quintuple layer terminations reflecting its alternating stacking sequence. MnBi_2Te_4 exhibits robust three-dimensional Ising-like critical behavior together with a distinct low-temperature first-order transition. In contrast, MnBi_4Te_7 displays crossover-dominated criticality arising from weakened interlayer exchange and competing magnetic phases. Correspondingly, the magnetocaloric response differs significantly between the two compounds. MnBi_2Te_4 shows dual-type magnetocaloric behavior with a sharp field-induced sign reversal of the isothermal magnetic entropy change ($-\Delta S_M$). It exhibits both inverse ($-\Delta S_M < 0$) and conventional ($-\Delta S_M > 0$) magnetocaloric effects. In contrast, MnBi_4Te_7 shows only conventional magnetocaloric response with a broad positive entropy peak. These results establish structural layering as a key parameter governing magnetic critical fluctuations and magnetocaloric behavior in $\text{MnBi}_{2n}\text{Te}_{3n+1}$ topological magnets.

1. INTRODUCTION

The $\text{MnBi}_{2n}\text{Te}_{3n+1}$ (MBT) family represents a unique class of intrinsic magnetic topological insulators (MTIs) that provide a rich platform to investigate the interplay between magnetism and nontrivial band topology within a van der Waals framework [1–5]. Within this family, MnBi_2Te_4 ($n = 1$) and MnBi_4Te_7 ($n = 2$) are key members [2]. MnBi_2Te_4 crystallizes in a rhombohedral layered structure with the septuple layer (SL) Te–Bi–Te–Mn–Te–Bi–Te as its fundamental building block [6–8]. In this configuration, Mn ions generate strong intralayer ferromagnetic (FM) coupling, while adjacent septuple layers couple antiferromagnetically (AFM), establishing an A-type AFM ground state [9–12]. In contrast, MnBi_4Te_7 forms a natural van der Waals heterostructure of magnetic MnBi_2Te_4 septuple and nonmagnetic Bi_2Te_3 quintuple layer (QL) layers [2, 13]. The presence of these nonmagnetic spacer layers weakens the interlayer exchange interactions relative to MnBi_2Te_4 [14, 15]. The tunable magnetic states in these layered systems enable diverse topological quantum phenomena including the quantum anomalous Hall effect, axion states and Weyl semimetal phases [16–19]. Thus, highlighting the MBT family as a central platform for studying topological magnetism [20, 21].

Although previous studies have mapped complex magnetic phase diagrams and metamagnetic transitions in detail [22–25], the precise influence of intercalated non-magnetic quintuple layers and structural complex-

ity on the magnetic critical fluctuations across the $\text{MnBi}_{2n}\text{Te}_{3n+1}$ family remains insufficiently explored [26]. While such structural modulation is known to modify magnetic anisotropy, spin-reorientation behavior, and phase stability [27–29], its quantitative impact on the divergence of correlation length, the strength of critical spin fluctuations, and the effective magnetic dimensionality near T_c remains unresolved [30, 31]. Resolving this issue is essential because critical fluctuations govern the universality class, entropy redistribution, and the stability of long-range magnetic coherence [32, 33], which in turn directly influences the stability of magnetism-driven topological phenomena such as the QAHE and axion insulators in these layered van der Waals magnetic systems [32–35].

Critical scaling analysis provides a direct and quantitative framework to probe these effects [36, 37]. Here, we extract the critical exponents β , γ , and δ , which characterize spontaneous magnetization growth, susceptibility divergence and field-dependent scaling near the transition [38]. In non-trivial magnetic systems, deviations from ideally known universality classes such as the three-dimensional Ising or Heisenberg values is often reported [25, 39, 40]. These deviations may indicate reduced effective dimensionality, incomplete development of critical fluctuations or competition between antiferromagnetic and field-induced ferromagnetic states [41–44]. Similarly, in higher- n compounds such as MnBi_4Te_7 , it is still unclear whether the structural dilution in MBT family preserves asymptotic three-dimensional criticality or instead drives a dimensional crossover toward suppressed fluctuations [45, 46].

Although critical scaling characterizes the evolution of magnetic fluctuations near ordering transitions, it does not directly probe the thermodynamic nature of

*Contact author: smanna@physics.iitd.ac.in

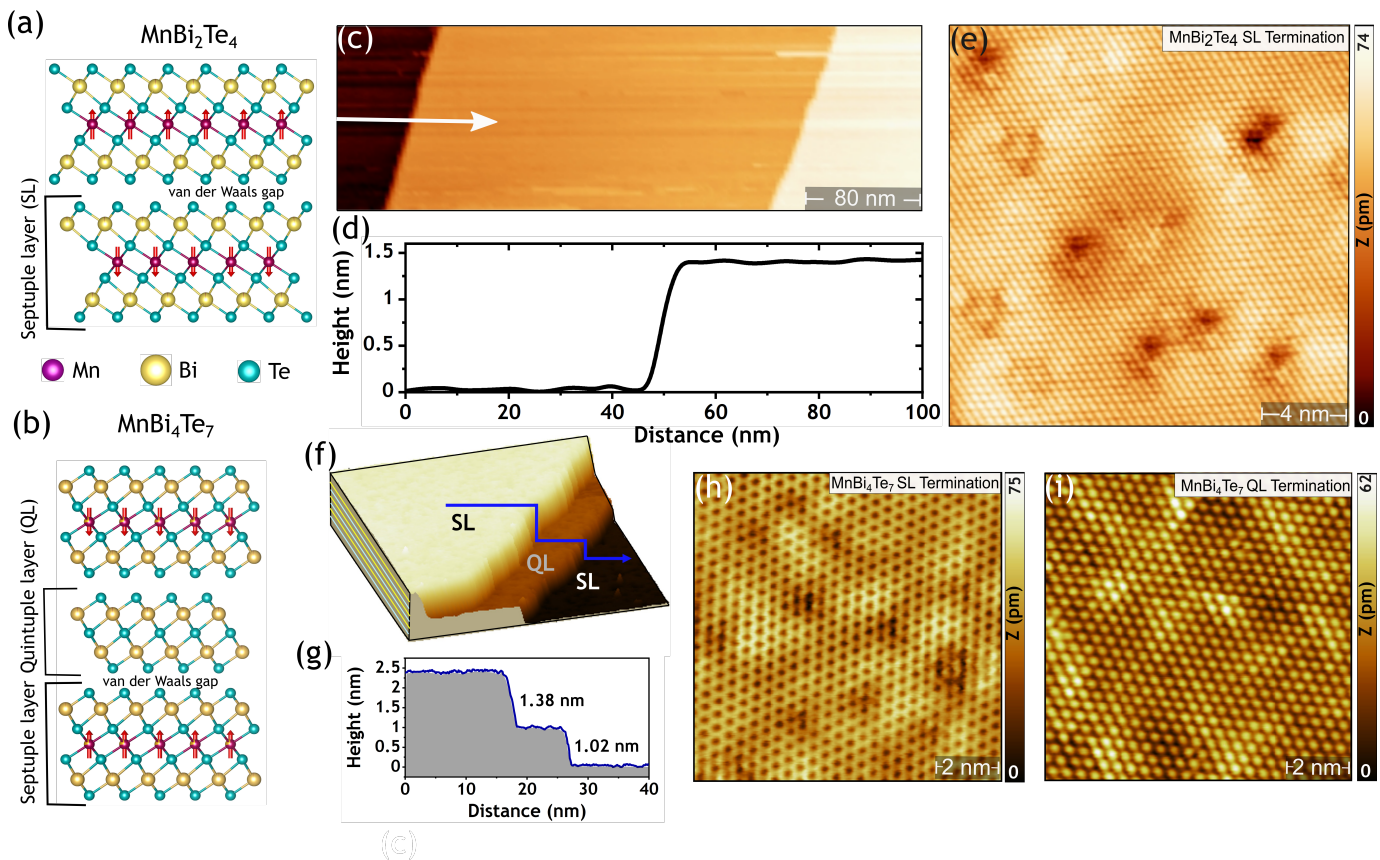


FIG. 1: (a) Crystal structure of MnBi_2Te_4 composed of septuple layers (SL) stacked along the c -axis. (b) Crystal structure of MnBi_4Te_7 , where MnBi_2Te_4 septuple layers alternate with Bi_2Te_3 quintuple layers (QL). (c) Large-scale ($400 \text{ nm} \times 400 \text{ nm}$) constant current STM topography ($U = 0.5 \text{ V}$, $I = 60 \text{ pA}$) obtained on freshly cleaved (0001) surface of MnBi_2Te_4 , displaying atomically flat terraces separated by sharp step edges. The height profile along the indicated direction yields a step height $\sim 1.41 \text{ nm}$ consistent with a single septuple-layer thickness as shown in (d). (e) Atomically-resolved STM image ($20 \text{ nm} \times 20 \text{ nm}$) of the SL-terminated surface of MnBi_2Te_4 , clearly depicting the hexagonal lattice of Te-terminated surface ($U = 150 \text{ mV}$, $I = 300 \text{ pA}$). (f) Large-scale STM topography ($50 \text{ nm} \times 50 \text{ nm}$) taken ($U = 900 \text{ mV}$, $I = 140 \text{ pA}$) of the Te-terminated (0001) surface of MnBi_4Te_7 , exhibiting terraces with two discrete step heights corresponding to distinct surface terminations. (g) Line profile across the step in (f), revealing step heights of $\sim 1.38 \text{ nm}$ and $\sim 1.02 \text{ nm}$, consistent with septuple- and quintuple-layer thicknesses, respectively. (h) High-resolution STM image ($10 \text{ nm} \times 10 \text{ nm}$) acquired on the SL-terminated terrace ($U = 500 \text{ mV}$, $I = 460 \text{ pA}$) of MnBi_4Te_7 . (i) Atomic-resolution STM image ($10 \text{ nm} \times 10 \text{ nm}$) acquired ($U = 400 \text{ mV}$, $I = 150 \text{ pA}$) on the QL-terminated terrace, both depicting the hexagonal Te-terminated surface lattice.

field-driven instabilities [47]. The magnetocaloric effect (MCE) provides a complementary thermodynamic probe by quantifying the isothermal entropy change or adiabatic temperature change induced by an applied magnetic field [48]. Therefore, using this complementary technique we can bridge the gap between structural layering, critical scaling behavior, and thermodynamic response in van der Waals MBT family.

Here, we present a systematic comparative study combining the atomic-resolution scanning tunneling microscopy, magnetic critical behavior and magnetocaloric response in MnBi_2Te_4 and MnBi_4Te_7 . Our analysis reveals that structural layering, determined by the number of nonmagnetic Bi_2Te_3 spacer layers, serves as a key parameter controlling the effective magnetic dimensionality and critical universality class. We further

show that this structural modulation strongly influences the magnetocaloric response of the two compounds and the nature of the magnetic phase transition across the $\text{MnBi}_{2n}\text{Te}_{3n+1}$ family.

2. EXPERIMENTAL METHODS

Single crystals of MnBi_2Te_4 and MnBi_4Te_7 were grown using self-flux method [2, 24]. High-purity Mn, Bi, and Te elements were weighed in the appropriate stoichiometric ratios, thoroughly mixed, pelletized and sealed in evacuated quartz ampoules. The sealed ampoules were heated to $900 \text{ }^\circ\text{C}$ and slowly cooled to $585 \text{ }^\circ\text{C}$ for MnBi_2Te_4 and $587 \text{ }^\circ\text{C}$ for MnBi_4Te_7 , followed by rapid quenching in water. The growth yielded shiny, plate-

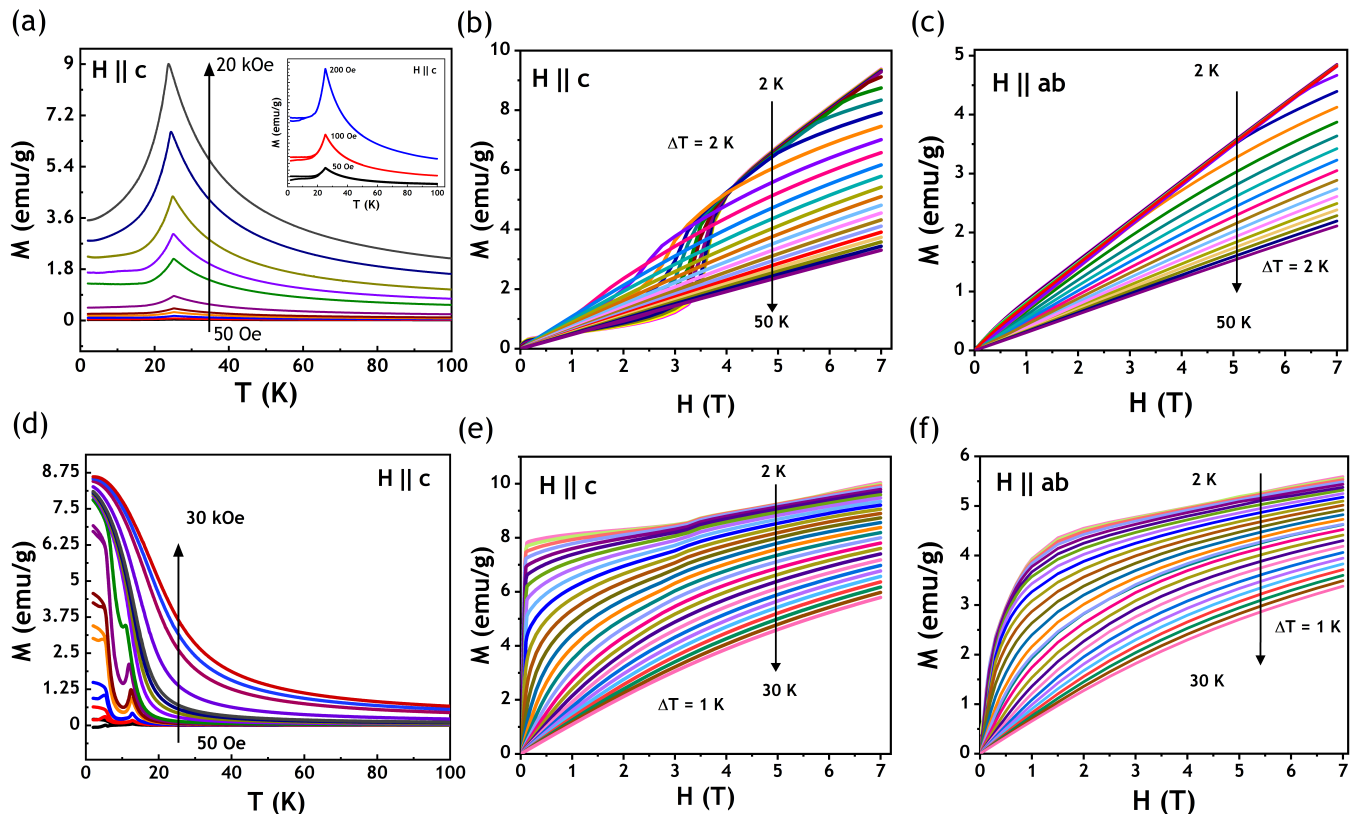


FIG. 2: (a) M - T curves of MnBi_2Te_4 single crystals under different magnetic field with $H \parallel c$. The anomaly at ~ 24.1 K marks the AFM transition. Inset: zoomed M - T curves for lower fields. (b, c) Isothermal magnetization of MnBi_2Te_4 , for $H \parallel c$ and $H \parallel ab$, respectively. We observe a metamagnetic transition (spin-flip) around 2-4 T in $H \parallel c$, evolving into a gradual response toward T_N in $H \parallel c$ configuration. (d) M - T curves of MnBi_4Te_7 single crystals under ZFC and FC with $H \parallel c$. The transition at ~ 12.9 K indicates layered AFM ordering. (e, f) Isothermal magnetization of MnBi_4Te_7 , for $H \parallel c$ and $H \parallel ab$, respectively. We observe a weak anomaly at lower temperatures and magnetic fields compared with MnBi_2Te_4 .

like layered crystals with typical dimensions of approximately $6 \times 4 \times 2 \text{ mm}^3$. Structural characterization was carried out using powder X-ray diffraction (XRD) and energy-dispersive X-ray (EDX) spectroscopy, confirming phase purity and stoichiometric composition. Magnetic measurements were performed using a Quantum Design MPMS3 magnetometer. Magnetization was measured in both zero-field-cooled (ZFC) and field-cooled (FC) protocols over a temperature range of 2–300 K under applied magnetic fields of up to 7 T.

To investigate the large-scale surface topography and atomic-scale morphology of the crystals, scanning tunneling microscopy (STM) measurements were performed. All STM experiments were carried out in an ultrahigh vacuum (UHV) commercial Unisoku low-temperature STM system operating at a base pressure of approximately 2×10^{-10} mbar [24]. Single crystals were cleaved *in situ* to expose fresh (0001) surfaces and were immediately transferred to the STM stage to minimize surface degradation. Measurements were conducted at 78 K using mechanically cut PtIr tips. Topographic images were acquired in the constant-current mode using tunneling set-point currents in the range of 50–500 pA and sample

bias voltages between 0.1 and 1.0 V.

3. RESULTS AND DISCUSSION

3.1. STM imaging of SL-QL layered structures

To probe the structural evolution across the $\text{MnBi}_{2n}\text{Te}_{3n+1}$ series, scanning tunneling microscopy (STM) measurements were performed on MnBi_2Te_4 ($n = 1$) and MnBi_4Te_7 ($n = 2$) under identical conditions. Large-area constant-current topographs of MnBi_2Te_4 [Fig. 1(c)] reveal atomically flat terraces separated by step edges of ~ 1.41 nm. This step height is consistent with the crystallographic septuple-layer (SL) thickness along the c axis, as verified by the line-profile analysis shown in Fig. 1(d). Atomic-resolution topography [Fig. 1(e)] resolves the hexagonal Te surface lattice on the (0001) termination. Thus, confirming the expected SL termination in MnBi_2Te_4 .

The large-area topography in MnBi_4Te_7 [Fig. 1(f)] reveals terraces separated by two distinct step heights. The corresponding height profile is shown in Fig. 1(g).

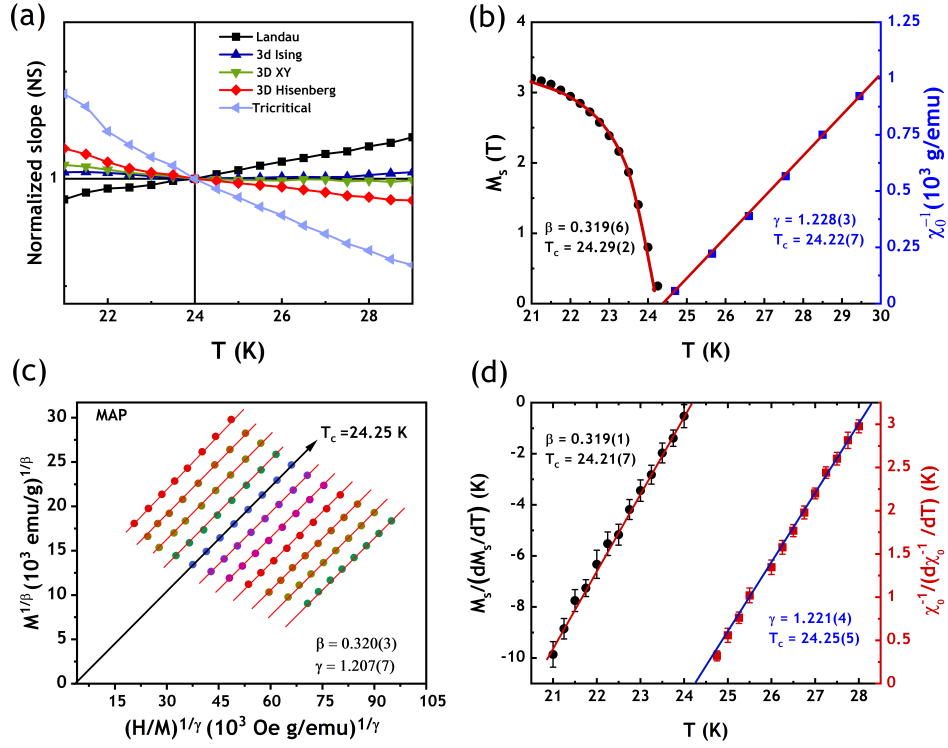


FIG. 3: Normalized slope of the Arrott plots as a function of temperature in MnBi_2Te_4 . (b) Temperature dependence of the spontaneous magnetization M_S (left axis) and the inverse initial susceptibility χ_0^{-1} (right axis) fitted with the power-law relations in Eqs. (3) and (5). The solid lines represent the best fits. (c) Modified Arrott plots ($M^{1/\beta}$ vs. $(H/M)^{1/\gamma}$) yields $\beta=0.319$ and $\gamma=1.221$. (d) Kouvel–Fisher plots of $M_S(dM_S/dT)^{-1}$ (left axis) and $\chi_0^{-1}(d\chi_0^{-1}/dT)^{-1}$ (right axis) as a function of temperature.

Two distinct step heights of approximately 1.38 nm and 1.02 nm are observed. Atomically-resolved STM images acquired on different terraces further confirm the surface terminations. Fig. 1(h) shows an atomic-scale topography obtained on the SL termination, where a well-ordered hexagonal Te surface lattice is clearly resolved. Moreover, Fig. 1(i) shows the atomic-scale topography of the Te-terminated QL surface. Therefore, the atomic-resolution of the SL-terminated Te surface in MnBi_2Te_4 and coexistence of the SL-QL terminations in MnBi_4Te_7 , provide direct real-space evidence of structural stacking for both compounds and are in good agreement with previous reports [8, 9, 24].

3.2. Critical scaling methodology

To investigate the nature of the magnetic phase transition in the MBT compounds, we first employed the conventional Arrott plot analysis, where M^2 is plotted as a function of H/M based on the mean-field framework. Within this model [49], the Arrott plots are expected to display a set of parallel straight lines in the high-field region, with the isotherm at T_c intersecting the origin. The sign of the slope provides a criterion for the transition order: a positive slope corresponds to a continuous

(second-order) transition, while a negative slope signals a discontinuous (first-order) transition [50]. As shown in Fig.S2(a) and Fig.S3(a), the isotherms for MnBi_2Te_4 and MnBi_4Te_7 exhibit positive slopes at high fields, suggesting a second-order magnetic transition. However, the nonlinearity and lack of parallelism in the curves indicate that the mean-field approximation fails to capture the critical behavior of the system.

To properly describe the critical region, we applied the Arrott–Noakes equation of state [51],

$$\left(\frac{H}{M}\right)^{1/\gamma} = a\varepsilon + bM^{1/\beta}, \quad (1)$$

where β and γ are the critical exponents associated with the spontaneous magnetization and the inverse susceptibility, respectively and a and b are constants. The reduced temperature is defined as

$$\varepsilon = \frac{T}{T_c} - 1 \quad (2)$$

From scaling theory, the critical behavior is further characterized by the relations

$$M_s(T) \propto (-\varepsilon)^\beta, \quad \varepsilon < 0 \quad (T < T_c), \quad (3)$$

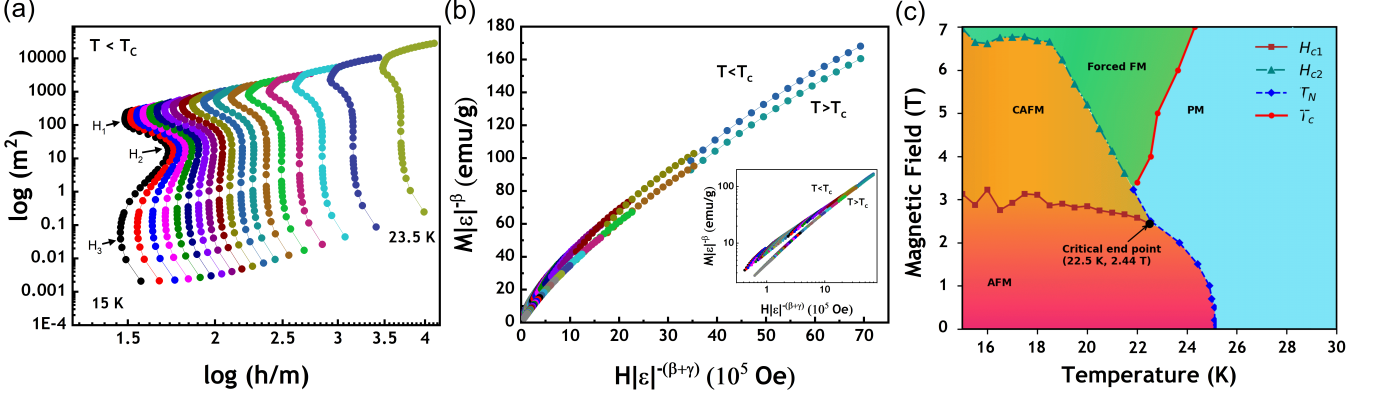


FIG. 4: (a) Scaling plots of the renormalized magnetization $M|\varepsilon|^{-\beta}$ versus renormalized field $H|\varepsilon|^{-(\beta+\gamma)}$ for MnBi_2Te_4 , confirms the validity of the critical exponents $\beta = 0.319$ and $\gamma = 1.221$. The inset shows the same data on a log–log scale, confirming consistency with the scaling hypothesis. (b) Enlarged view of the low-temperature region of the log–log Renormalized Arrott Plots, where arrows indicate characteristic phase-boundary points. (c) Magnetic phase diagram of MnBi_2Te_4 obtained by combining the results from the renormalized Arrott plot (RAP) analysis with field-dependent magnetization measurements.

$$M(H) \propto H^{1/\delta}, \quad \varepsilon = 0 \quad (T = T_c), \quad (4)$$

$$\chi_0^{-1}(T) \propto \varepsilon^\gamma, \quad \varepsilon > 0 \quad (T > T_c) \quad (5)$$

where β , γ , and δ correspond to the exponents governing the spontaneous magnetization, the initial susceptibility, and the critical isotherm, respectively.

Since the standard Arrott plots are inadequate, we constructed modified Arrott plots (MAPs) of $M^{1/\beta}$ versus $(H/M)^{1/\gamma}$ using trial values of the exponents corresponding to various universality classes, such as the 2D Ising ($\beta = 0.125$, $\gamma = 1.75$), 3D Heisenberg ($\beta = 0.365$, $\gamma = 1.386$), 3D XY ($\beta = 0.345$, $\gamma = 1.316$), 3D Ising ($\beta = 0.325$, $\gamma = 1.24$), and tricritical mean-field ($\beta = 0.25$, $\gamma = 1.0$) (Fig S2 (b - f) and S3 (b - f)). To quantify the accuracy of each model, we used the normalized slope (NS) method: $NS(T) = \frac{S(T)}{S(T_c)}$, $S(T) = \left(\frac{dM^{1/\beta}}{d(H/M)^{1/\gamma}} \right)$. An ideal model would produce parallel isotherms with $NS \approx 1$ near T_c . The representative figures for both the samples are shown in Fig. 3(a) and Fig. 5(a), respectively.

The inadequacy of predefined universality classes motivates a model-independent determination of critical exponents. We therefore implemented a modified iterative method (MIM), following approaches developed for systems exhibiting crossover behavior [39, 52]. Starting with trial β and γ values, we obtained $M_s(T)$ and $\chi_0^{-1}(T)$ by linear extrapolation of the high-field portions of the MAPs to the respective axes. The resulting data were fitted using Eqs. (3) and (5) to refine the exponents. The ordered- and paramagnetic-branch data were then fitted separately to their respective power laws to update β , γ , and T_c . The procedure was iterated until convergence, which is defined by stable exponent values and parallel high-field isotherms. This two-sided scheme enables the detection of asymmetric effective exponents and is par-

ticularly suited for systems exhibiting crossover phenomena. The modified plots were then reconstructed with the updated values, and the process was repeated until convergence was achieved. This self-consistent method yielded stable values of β and γ , independent of the initial guess, confirming the robustness of the obtained exponents. The final MAPs, shown in Fig.3(b, c) and Fig.5(b), display a series of nearly parallel straight lines in the critical region, thereby validating the reliability of the extracted critical parameters for MnBi_2Te_4 and MnBi_4Te_7 .

To further validate the exponents, we performed Kouvel–Fisher (KF) analysis, where the relations [37]

$$\frac{M_S(T)}{dM_S(T)/dT} = \frac{T - T_C}{\beta}, \quad (6)$$

$$\frac{\chi_0^{-1}(T)}{d\chi_0^{-1}(T)/dT} = \frac{T - T_C}{\gamma}, \quad (7)$$

yield straight lines whose slopes provide independent estimates of β and γ . The KF plots [Fig.3(d) and S4(c)] are in good agreement with the MAP results. The critical isotherm at T_c , plotted on a log–log scale follows the relation

$$M \propto H^{1/\delta}, \quad (8)$$

from which we obtain δ . The consistency of the Critical exponents can be further checked using the Widom relation,

$$\delta = 1 + \frac{\gamma}{\beta}, \quad (9)$$

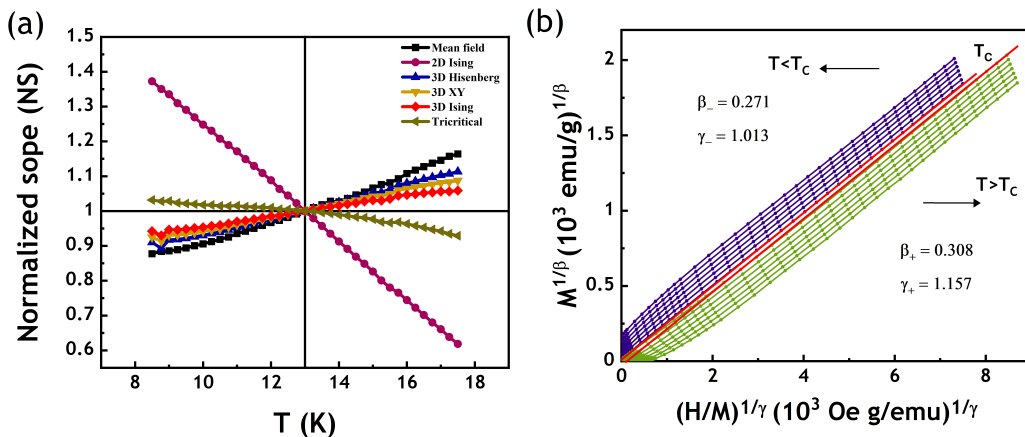


FIG. 5: (a) Normalized slope of the Arrott plots as a function of temperature in MnBi_4Te_7 . (b) Modified Arrott plots (MAPs) constructed using the critical exponents obtained from the modified iteration method.

We verified the reliability of the critical exponents by performing a scaling analysis of the magnetization isotherms near T_c . According to the scaling hypothesis, the equation of state close to the critical point can be written as

$$M(H, \varepsilon) = |\varepsilon|^\beta f_\pm \left(\frac{H}{|\varepsilon|^{\beta+\gamma}} \right), \quad (10)$$

where $\varepsilon = (T - T_c)/T_c$ is the reduced temperature and f_\pm denotes the scaling functions for $T < T_c$ and $T > T_c$. In Fig. 4(a) and Fig. 6(a), we plot $M|\varepsilon|^{-\beta}$ as a function of $H|\varepsilon|^{-(\beta+\gamma)}$ for MnBi_2Te_4 and MnBi_4Te_7 , respectively. While Fig. 6(b) shows the renormalized form m^2 versus h/m , where $m = M|\varepsilon|^{-\beta}$ and $h = H|\varepsilon|^{-(\beta+\gamma)}$. The collapse of the isotherms into two distinct branches corresponding to $T < T_c$ and $T > T_c$ confirms the internal consistency of the extracted critical exponents. This excellent scaling behavior provides compelling evidence that the magnetic phase transition in both samples around the transition temperature is of second order, in agreement with the predictions of the scaling theory.

As we know, for a homogeneous magnet, the universality class of the magnetic phase transition depends on the nature of the exchange interaction $J(r)$. Fisher *et al.* theoretically treated this kind of ordering as an attractive interaction of spins, where a renormalization-group analysis suggests that the exchange interaction decays with distance r as [37]

$$J(r) \sim r^{-(d+\sigma)}, \quad (11)$$

where σ is a positive constant. Moreover, the susceptibility exponent γ is predicted as [37].

$$\begin{aligned} \gamma = 1 + \frac{4}{d} \left(\frac{n+2}{n+8} \right) \Delta\sigma \\ + \frac{8(n+2)(n-4)}{d^2(n+8)^2} \left[1 + \frac{2G(d/2)}{d} \right] \frac{(7n+20)}{(n-4)(n+8)} (\Delta\sigma)^2. \end{aligned} \quad (12)$$

where $\Delta\sigma = \sigma - d/2$, $G(d/2) = 3 - \frac{1}{4}(d/2)^2$, d is the spatial dimension, and n is the spin dimensionality.

3.3. Critical behavior of MnBi_2Te_4 and MnBi_4Te_7

In MnBi_2Te_4 , the spontaneous magnetization $M_s(T)$ and inverse initial susceptibility $\chi_0^{-1}(T)$ were obtained from the intercepts of the high-field Arrott isotherms [Fig. 3(b)] and analyzed using the Kouvel–Fisher method [Fig. 3(d)]. This analysis yields the critical exponents $\beta \approx 0.319$ and $\gamma \approx 1.221$, together with a consistent transition temperature $T_c \approx 24.25$ K. The reliability of these exponents is further supported by scaling analysis, where the magnetization data collapse onto two universal branches above and below T_c as shown in Fig. 4(a). The obtained values are close to those expected for the three-dimensional Ising universality class, indicating strong easy-axis anisotropy in MnBi_2Te_4 . Further insight into the field evolution of the magnetic state is obtained from the renormalized Arrott plots shown on a log–log scale in Fig. 4(b). The systematic evolution of the curves with temperature reflects the field-driven modification of the antiferromagnetic order. Combining these results with field-dependent magnetization measurements allows the construction of the magnetic phase diagram of MnBi_2Te_4 , Fig. 4(c).

The critical behavior of MnBi_4Te_7 differs from that of MnBi_2Te_4 , reflecting the reduced magnetic connectivity introduced by the insertion of nonmagnetic Bi_2Te_3 quintuple layers. Separate fits above and below T_c yield distinct effective critical exponents: for $T < T_c$, $\beta^- \approx 0.271$ and $\gamma^- \approx 1.013$, while for $T > T_c$ we obtain $\beta^+ \approx 0.308$ and $\gamma^+ \approx 1.157$ Fig. 5(b). The asymmetry of the exponent sets indicates that the transition is not governed by a single universal class.

Furthermore, Fig. 6 depicts the scaling analysis of the magnetization data, which supports this conclusion. A single set of critical exponents fails to collapse the data

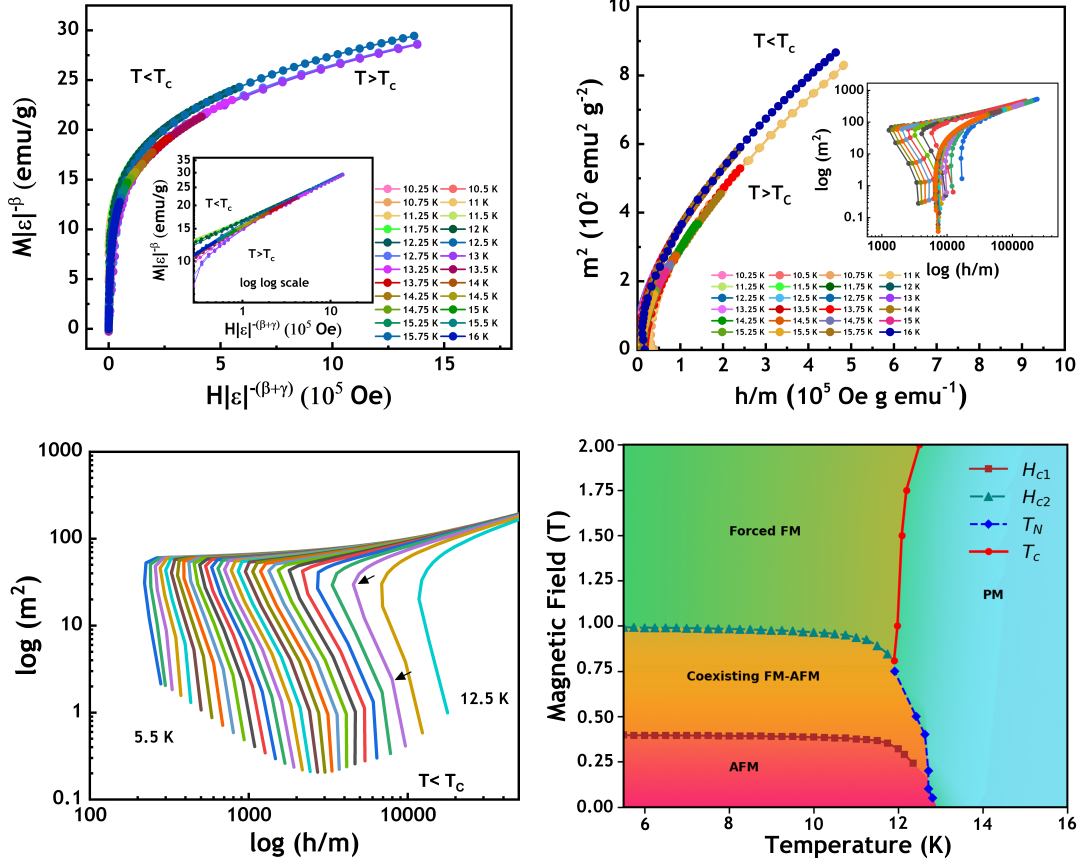


FIG. 6: (a) Scaled magnetization data of MnBi $_4$ Te $_7$ analyzed within the framework of the magnetic equation of state. The data collapse onto two separate branches below and above T_c , confirms the validity of the critical exponents $\beta^- \approx 0.271$, $\gamma^- \approx 1.013$ below T_c and $\beta^+ \approx 0.308$, $\gamma^+ \approx 1.157$ above T_c . The inset shows the same data on a log–log scale, which confirms consistency with the scaling hypothesis. (b) Scaling collapse of the renormalized magnetization and field, m^2 vs h^2 , is in good agreement for both $T < T_c$ and $T > T_c$. (c) Enlarged view of the low-temperature region of the log–log RAP, where arrows schematically indicate characteristic phase-boundary points. (d) Magnetic phase diagram of MnBi $_4$ Te $_7$.

over the entire temperature range [Fig. S4(a)], whereas separate scaling above and below T_c yields improved agreement [Fig. 5(b)]. Such behavior is characteristic of crossover-dominated criticality, which can be attributed to weakened interlayer exchange and the proximity of a low-field tricritical point reported near 11.9 K and 750 Oe [22]. The combined influence of reduced magnetic coherence and tricritical fluctuations suppresses the asymptotic critical region, resulting in effective exponent values that vary across the transition.

Moreover, our previous work [24] reveals a frequency-dependent anomaly near 6 K, indicating freezing of ferromagnetic clusters within an antiferromagnetic matrix. Thus, while the transition near T_c reflects antiferromagnetic ordering, the low-temperature state is governed by cluster-driven magnetic dynamics.

To probe the spatial range of magnetic interactions, we analyze the critical exponents within the renormalization-group framework for long-range exchange $J(r) \sim r^{-(d+\sigma)}$. Assuming $d = 3$ and Ising spin symmetry ($n = 1$), the measured exponents yield

$\sigma \approx 1.88$ for MnBi $_2$ Te $_4$, corresponding to $J(r) \sim r^{-4.88}$. For MnBi $_4$ Te $_7$, the values $\beta_- \approx 0.271$, $\gamma_- \approx 1.013$ give $\sigma_- \approx 1.53$ below T_c , while $\beta_+ \approx 0.308$, $\gamma_+ \approx 1.157$ yield $\sigma_+ \approx 1.80$ above T_c , corresponding to $J(r) \sim r^{-4.53}$ and $J(r) \sim r^{-4.80}$, respectively.

The range $1.5 < \sigma < 2$ places both systems in the crossover regime between long-range and short-range magnetic interactions, indicating intermediate-range exchange. Moreover, we observe a slower spatial decay of the exchange interaction in MnBi $_4$ Te $_7$ compared with MnBi $_2$ Te $_4$, implying a slightly longer effective interaction range in MnBi $_4$ Te $_7$. This behavior likely originates from the insertion of the Bi $_2$ Te $_3$ quintuple layer, which modifies the interlayer exchange pathways within the MnBi $_2n$ Te $_{3n+1}$ structure.

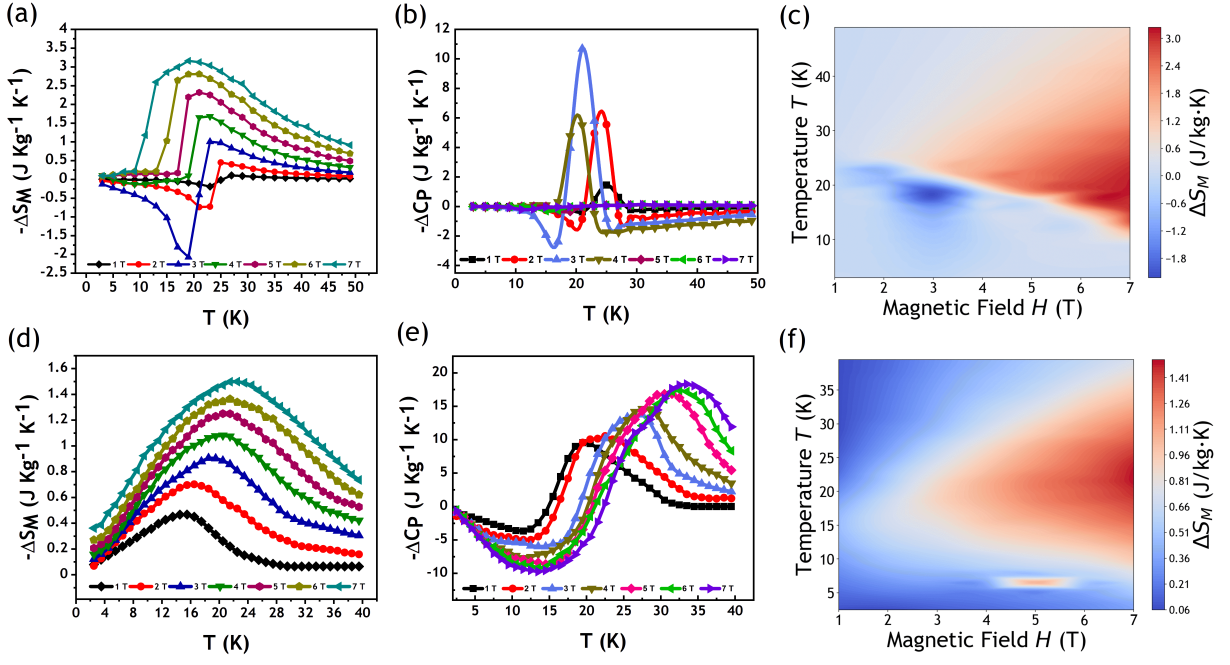


FIG. 7: (a, d) Temperature dependence of the magnetic entropy change $-\Delta S_M(T, H)$ for MnBi_2Te_4 and MnBi_4Te_7 , respectively, calculated from magnetization isotherms for fields ranging from 1 to 7 T. MnBi_2Te_4 exhibits a dual magnetocaloric response with a positive entropy peak near T_c (≈ 24.25 K) and a inverse entropy pocket at lower temperatures associated with field-induced spin-flip transitions. In contrast, MnBi_4Te_7 shows a broad and predominantly positive entropy change centered near T_c (≈ 13.05 K). (b, e) Temperature dependence of the field-induced heat-capacity change $-\Delta C_P(T, H)$ for MnBi_2Te_4 and MnBi_4Te_7 , respectively. MnBi_2Te_4 displays sharp field-enhanced anomalies near T_c , whereas MnBi_4Te_7 exhibits broader variations extending over a wider temperature range. (c, f) Contour maps of the magnetic entropy change $\Delta S_M(T, H)$ for MnBi_2Te_4 and MnBi_4Te_7 , illustrating the evolution of entropy with temperature and magnetic field. The contour map of MnBi_2Te_4 reveals a distinct region of negative entropy change at intermediate fields and low temperatures, while MnBi_4Te_7 shows a smooth, predominantly positive entropy distribution.

3.4. Magnetocaloric signatures of MnBi_2Te_4 and MnBi_4Te_7

The magnetocaloric effect (MCE) originates from the coupling between the magnetic entropy and the external magnetic field, and provides valuable information about the nature of magnetic interactions and phase transitions. The isothermal magnetic entropy change, $\Delta S_M(T, H)$, can be obtained from the magnetization isotherms using Maxwell's relation, which connects the entropy S with the magnetization M as [53, 54]

$$\left(\frac{\partial S}{\partial H}\right)_T = \left(\frac{\partial M}{\partial T}\right)_H. \quad (13)$$

Integrating over the magnetic field yields

$$\Delta S_M(T, \Delta H) = \int_0^{\Delta H} \left(\frac{\partial M}{\partial T}\right)_H dH, \quad (14)$$

where ΔH is the change in magnetic field. In practice, for a discrete set of isothermal $M(H)$ curves measured at successive temperatures, the entropy change

$-\Delta S_M(T, H)$ can be approximated as [54]

$$\left|\Delta S_M\left(\frac{T_i + T_{i+1}}{2}, H\right)\right| = \sum_i \left[\frac{(M_{i+1} - M_i)}{T_{i+1} - T_i}\right] \Delta H_i. \quad (15)$$

Also, the magnetic contribution to the specific heat can be derived from entropy as [54]

$$\Delta C_p(T, H) = C_p(T, H) - C_p(T, 0) = T \frac{\partial \Delta S_M(T, H)}{\partial T}. \quad (16)$$

For MnBi_2Te_4 [Fig. 7(a)], the isothermal magnetic entropy change $-\Delta S_M(T)$ displays a dual behaviour. At low applied fields ($\mu_0 H = 1-3$ T), we observe a negative entropy contribution around 15-18 K, indicating an inverse magnetocaloric effect. As the field is increased ($\mu_0 H = 4-7$ T), the entropy change undergoes a well-defined sign inversion and shows conventional magnetocaloric effect with a sharp positive peak around $T_c \sim 24.25$. For a maximum field change $\Delta H = 7$ T the peak magnitude reaches $-\Delta S_M^{\max} \approx 3 \text{ J kg}^{-1} \text{ K}^{-1}$. The pronounced asymmetry and field-dependent switching of entropy change is consistent with a field-induced reorientation spin-flip transition of MnBi_2Te_4 , which produces

a rapid redistribution of magnetic entropy. The contour map of $-\Delta S_M(T, H)$ [Fig. 7(c)] further highlights this behavior by revealing a distinct region of negative entropy change within the same temperature and field window.

In contrast, MnBi_4Te_7 [Fig. 7(d)] exhibits a qualitatively different magnetocaloric behavior. The entropy change remains positive across the measured temperature range and evolves smoothly with increasing field, producing a single, broad maximum centered near the $T_c \sim 13.05$ K. The peak magnitude increases monotonically with field and attains $-\Delta S_M^{\text{max}} \approx 1.5 \text{ J kg}^{-1} \text{ K}^{-1}$ for $\Delta H = 7$ T. The absence of entropy sign reversal and the broad temperature distribution of the entropy peak indicate a more gradual field-driven polarization of moments rather than an abrupt metamagnetic reorientation. The corresponding contour map [Fig. 7(f)] indicates that the entropy change remains predominantly positive throughout the explored temperature and field range. The absence of negative entropy regions and sharp thermodynamic anomalies suggests that field-induced spin-flip processes are significantly suppressed in MnBi_4Te_7 .

These entropy trends are further supported by the field-dependent heat-capacity change $\Delta C_P(T, H)$. In MnBi_2Te_4 [Fig. 7(b)], ΔC_P shows sharp field-enhanced peaks near the magnetic ordering temperature (~ 20 – 25 K). This behavior reflects strong thermodynamic fluctuations close to the transition. In contrast, MnBi_4Te_7 [Fig. 7(e)] shows a broader and more gradual variation of $\Delta C_P(T, H)$ over a wider temperature range (~ 10 – 35 K). The heat-capacity change increases smoothly with field and does not show the sharp anomalies seen in MnBi_2Te_4 . This broader response indicates that magnetic entropy is redistributed over a wider temperature range. Such behavior is consistent with reduced effective interlayer coupling and the coexistence of ferromagnetic and antiferromagnetic correlations in MnBi_4Te_7 reported in earlier studies [24].

From an application perspective, the sharp entropy variations of MnBi_2Te_4 make it a strong candidate for low-temperature magnetocaloric cooling and field-tunable spintronic switches that exploit discrete transitions. MnBi_4Te_7 , with smoother tunability and reduced coercivity, is better suited for reversible, low-energy manipulation of topological states. Together, these results establish the MBT family as a versatile materials platform where layer engineering directly controls the interplay between magnetism, entropy, and topology, enabling

pathways to realize QAHE and related quantum phases in van der Waals magnets.

4. CONCLUSION

We presented the critical behavior and magnetocaloric properties of MnBi_2Te_4 and MnBi_4Te_7 to elucidate how structural layering in the $\text{MnBi}_{2n}\text{Te}_{3n+1}$ series controls magnetic interactions. STM reveals atomically flat septuple-layer terraces in MnBi_2Te_4 , whereas coexisting septuple and quintuple layer terminations in MnBi_4Te_7 . Critical-scaling analysis of the magnetization data yields distinct sets of critical exponents for the two compounds, which indicates different effective ranges of magnetic exchange and therefore different universality classes. Furthermore, magnetocaloric measurements provide complementary thermodynamic evidence. MnBi_2Te_4 displays both conventional and inverse magnetocaloric responses, whereas MnBi_4Te_7 displays a single, broad maximum and smoothly varying features in the entropy change ($-\Delta S_M(T, H)$). Altogether, the combined critical scaling and magnetocaloric results identify structural layering as a tunable parameter that controls magnetic dimensionality, the effective interaction range, and the thermodynamic pathways for entropy redistribution in this family. Extending the same analysis to higher- n members of $\text{MnBi}_{2n}\text{Te}_{3n+1}$ can show how the family evolves from three-dimensional criticality toward quasi-two-dimensional crossover behavior and will have direct implications for magnetically driven topological phenomena such as QAHE and axion electrodynamics in these materials.

5. ACKNOWLEDGMENTS

We thank Subhasis Ghosh (JNU), Martin Weigel and Christoph Tegenkamp (TUC) for insightful discussions. N.F. acknowledges financial support from the DST INSPIRE Fellowship (IF200582), Government of India. N.F. and S.M. acknowledge partial support of the Indo-German project SPARC-GIANT. The authors gratefully acknowledge the Department of Physics and the Central Research Facility (CRF), IIT Delhi, for MPMS and STM measurements.

-
- [1] M. Z. Hasan and C. L. Kane, Colloquium: Topological insulators, *Rev. Mod. Phys.* **82**, 3045 (2010).
 - [2] K. He, MnBi_2Te_4 -family intrinsic magnetic topological materials, *npj Quantum Materials* **5**, 90 (2020).
 - [3] Y. Tokura, K. Yasuda, and A. Tsukazaki, Magnetic topological insulators, *Nat. Rev. Phys.* **1**, 126 (2019).
 - [4] J. Li, Y. Li, W. Duan, Y. Xu, and S.-C. Zhang, In-

trinsic magnetic topological insulators in van der waals layered MnBi_2Te_4 -family materials, *Science Advances* **5**, eaaw5685 (2019).

- [5] M. M. Otrokov, I. I. Klimovskikh, H. Bentmann, D. Etyunin, A. Zeugner, Z. S. Aliev, S. Gaß, A. U. B. Wolter, A. V. Koroleva, A. M. Shikin, M. Blanco-Rey, M. Hoffmann, I. P. Rusinov, M. G. Vergniory, A. Kimura,

- L. Petaccia, G. Di Santo, R. C. Vidal, S. Schatz, K. Kißner, M. Ünzelmann, C. H. Min, S. Moser, T. R. F. Peixoto, F. Reinert, A. Ernst, P. M. Echenique, A. Isaeva, and E. V. Chulkov, Prediction and observation of an antiferromagnetic topological insulator, *Nature* **576**, 416 (2019).
- [6] X. Xu, S. Yang, H. Wang, R. Guzman, Y. Gao, Y. Zhu, Y. Peng, Z. Zang, M. Xi, S. Tian, Y. Li, H. Lei, Z. Luo, J. Yang, Y. Wang, T. Xia, W. Zhou, Y. Huang, and Y. Ye, Ferromagnetic-antiferromagnetic coexisting ground state and exchange bias effects in MnBi_4Te_7 and $\text{MnBi}_6\text{Te}_{10}$, *Nature Communications* **13**, 7646 (2022).
- [7] L. Ding, X. Wang, S. Xu, and Y. Li, Crystal and magnetic structures of MnBi_4Te_7 : A layered magnetic topological material, *Phys. Rev. B* **101**, 020412 (2020).
- [8] Y. Yuan, X. Wang, H. Li, J. Li, Y. Ji, Z. Hao, Y. Wu, K. He, Y. Wang, Y. Xu, *et al.*, Electronic states and magnetic response of MnBi_2Te_4 by scanning tunneling microscopy and spectroscopy, *Nano letters* **20**, 3271 (2020).
- [9] X. Wu, J. Li, X.-M. Ma, Y. Zhang, Y. Liu, C.-S. Zhou, J. Shao, Q. Wang, Y.-J. Hao, Y. Feng, *et al.*, Distinct topological surface states on the two terminations of MnBi_4Te_7 , *Physical Review X* **10**, 031013 (2020).
- [10] J. Cui, Y. Zhang, and Z. Wang, Layer-dependent magnetism and anomalous hall effect in MnBi_4Te_7 thin flakes, *Nano Lett.* **23**, 1234 (2023).
- [11] W. Ge, H. Wu, and J. Liu, Surface spin-flip transitions in MnBi_4Te_7 revealed by spectroscopy, *Phys. Rev. Lett.* **129**, 107204 (2022).
- [12] T. Kim, S. Lee, and H. Kwon, Layer-controlled topological phase transitions in MnBi_4Te_7 , *Nat. Commun.* **15**, 10.1038/s41467-024-10234-5 (2024).
- [13] C. Hu, T. Qian, and N. Ni, Recent progress in $\text{MnBi}_{2n}\text{Te}_{3n+1}$ intrinsic magnetic topological insulators: Crystal growth, magnetism, and chemical disorder, *National Science Review* **11**, nwad282 (2024).
- [14] J. Guo, H. Wang, H. Zhang, S. Mi, S. Li, H. Dong, S. Zhu, J. Hu, X. Wang, Y. Li, *et al.*, Interlayer coupling modulated tunable magnetic states in superlattice $\text{MnBi}_2\text{Te}_4(\text{Bi}_2\text{Te}_3)_n$ topological insulators, *Physical Review B* **109**, 165410 (2024).
- [15] M. Z. Shi, B. Lei, C. S. Zhu, D. H. Ma, J. H. Cui, Z. L. Sun, H. Chen, Y. Y. Wang, T. Zhang, Q. Li, and X. H. Chen, Magnetic and transport properties in the magnetic topological insulators $\text{MnBi}_2\text{Te}_4(\text{Bi}_2\text{Te}_3)_n$ ($n = 1, 2$), *Physical Review B* **100**, 155144 (2019).
- [16] Y. Deng, Y. Yu, M.-Z. Shi, Z. Guo, Z. Xu, J. Wang, X. Chen, and Y. Zhang, Quantum anomalous hall effect in intrinsic magnetic topological insulator MnBi_2Te_4 , *Science* **367**, 895 (2020).
- [17] D. Zhang, M. Shi, T. Zhu, D. Xing, H. Zhang, and J. Wang, Topological axion states in the magnetic insulator MnBi_2Te_4 with the quantized magnetoelectric effect, *Physical review letters* **122**, 206401 (2019).
- [18] M. Gibertini, M. Koperski, A. F. Morpurgo, and K. S. Novoselov, Magnetic 2d materials and heterostructures, *Nature Nanotechnology* **14**, 408 (2019).
- [19] A. Gao, Y. F. Liu, C. Hu, J. X. Qiu, C. Tzschaschel, B. Ghosh, P. Liu, J. Liu, Y. Liu, Y. Liu, R. Tang, S. Wang, X. Wang, Q. Ma, C. Liu, P. Jarillo-Herrero, N. Gedik, Q. Liu, T.-R. Chang, and S. Y. Xu, Layer hall effect in a 2d topological axion antiferromagnet, *Nature* **595**, 521 (2021).
- [20] Y. Zhao and Q. Liu, Routes to realize the axion-insulator phase in $\text{MnBi}_2\text{Te}_4(\text{Bi}_2\text{Te}_3)_n$ family, *Applied Physics Letters* **119**, 060502 (2021).
- [21] S. Li, M. Gong, S. Cheng, H. Jiang, and X. C. Xie, Dissipationless layertronics in axion insulator MnBi_2Te_4 , *National Science Review* **11**, nwad262 (2024).
- [22] H. Zhang, H. Wu, D. Liu, J. Huang, F. Gao, T. Yang, X. Zhao, B. Li, S. Ma, and Z. Zhang, Metamagnetic tricritical behavior of the magnetic topological insulator MnBi_4Te_7 , *Physical Review B* **109**, 214428 (2024).
- [23] T. Das and S. Mukhopadhyay, Metamagnetic quantum criticality in the antiferromagnetic topological insulator MnBi_2Te_4 , *Physical Review B* **111**, 174420 (2025).
- [24] N. Firdosh, S. Sinha, I. Sinha, M. Singh, S. Patnaik, and S. Manna, Exchange bias and anomalous hall effect driven by intertwined magnetic phases in MnBi_4Te_7 , *Physical Review B* **112**, 144410 (2025).
- [25] X. Yang, J. Pan, X. He, and D. Chu, Critical behavior, magnetic phase diagram, and magnetic entropy change of MnSb_4Te_7 , *Physical Review B* **109**, 094408 (2024).
- [26] L. Ding, C. Hu, E. Feng, C. Jiang, I. A. Kibalin, A. Gukasov, and H. Cao, Neutron diffraction study of magnetism in van der waals layered $\text{MnBi}_{2n}\text{Te}_{3n+1}$, *Journal of Physics D: Applied Physics* **54**, 174003 (2021).
- [27] Y. Sun, L. Zhang, and H. Li, Axion electrodynamics in antiferromagnetic topological insulators, *Phys. Rev. Materials* **7**, 074204 (2023).
- [28] Q. He, M. Li, and X. Xu, Van der waals magnets for next-generation quantum technologies, *J. Mater. Chem. C* **10**, 13214 (2022).
- [29] I. I. Klimovskikh, M. M. Otrokov, D. Estyunin, S. V. Ereemeev, S. O. Filnov, A. Koroleva, A. Isaeva, K. Kißner, M. Ünzelmann, C. H. Min, S. Moser, T. R. F. Peixoto, F. Reinert, A. Ernst, P. M. Echenique, and E. V. Chulkov, Tunable 3d/2d magnetism in the $\text{MnBi}_2\text{Te}_4(\text{Bi}_2\text{Te}_3)_m$ topological insulators family, *npj Quantum Materials* **5**, 54 (2020).
- [30] H.-K. Xu, M. Gu, F. Fei, Y.-S. Gu, D. Liu, Q.-Y. Yu, S.-S. Xue, X.-H. Ning, B. Chen, H. Xie, *et al.*, Observation of magnetism-induced topological edge state in antiferromagnetic topological insulator MnBi_4Te_7 , *ACS nano* **16**, 9810 (2022).
- [31] R. C. Vidal, A. Zeugner, J. I. Facio, R. Ray, M. H. Haghghi, A. U. Wolter, L. T. Corredor Bohorquez, F. Cagliaris, S. Moser, T. Figgemeier, *et al.*, Topological electronic structure and intrinsic magnetization in MnBi_4Te_7 : a Bi_2Te_3 derivative with a periodic mn sublattice, *Physical Review X* **9**, 041065 (2019).
- [32] W. B. Cui, W. Liu, W. J. Gong, X. H. Liu, S. Guo, F. Yang, and Z. D. Zhang, Exchange coupling in hard/soft-magnetic multilayer films with non-magnetic spacer layers, *Journal of Applied Physics* **111**, 07B533 (2012).
- [33] B. Li, D. M. Pajerowski, J. Q. Yan, and R. J. McQueeney, Role of nonmagnetic spacers in the magnetic interactions of antiferromagnetic topological insulators MnBi_4Te_7 and MnBi_2Te_4 , *Physical Review B* **111**, 064418 (2025).
- [34] L. Yang, J. Wu, and Q. Liu, High-temperature chern insulators in layered MnBi_4Te_7 , *Adv. Electron. Mater.* **9**, 2201280 (2023).
- [35] B. Zhao, Y. Liu, and P. Wang, Manipulating spin textures in layered magnetic topological insulators, *Phys. Rev. B* **108**, 094423 (2023).
- [36] M. E. Fisher, The theory of equilibrium critical phenomena, *Reports on progress in physics* **30**, 615 (1967).

- [37] M. E. Fisher, S.-k. Ma, and B. Nickel, Critical exponents for long-range interactions, *Physical Review Letters* **29**, 917 (1972).
- [38] V. Franco and A. Conde, Scaling laws for the magnetocaloric effect in second order phase transitions: From physics to applications for the characterization of materials, *international journal of refrigeration* **33**, 465 (2010).
- [39] H. C. Chauhan, B. Kumar, A. Tiwari, J. K. Tiwari, and S. Ghosh, Different critical exponents on two sides of a transition: Observation of crossover from ising to heisenberg exchange in skyrmion host Cu_2OSeO_3 , *Physical Review Letters* **128**, 015703 (2022).
- [40] L. Zhang, H. Han, M. Ge, H. Du, C. Jin, W. Wei, J. Fan, C. Zhang, L. Pi, and Y. Zhang, Critical phenomenon of the near room temperature skyrmion material fege, *Scientific reports* **6**, 22397 (2016).
- [41] F. Meng, W. Liu, A. Rahman, J. Zhang, J. Fan, C. Ma, M. Ge, T. Yao, L. Pi, L. Zhang, *et al.*, Crossover of critical behavior and nontrivial magnetism in the chiral soliton lattice host $\text{Cr}_{1/3}\text{TaS}_2$, *Physical Review B* **107**, 144425 (2023).
- [42] Y. Liu, M. Abeykoon, and C. Petrovic, Critical behavior and magnetocaloric effect in VI_3 , *Physical Review Research* **2**, 013013 (2020).
- [43] Y. Liu, V. N. Ivanovski, and C. Petrovic, Critical behavior of the van der waals bonded ferromagnet $\text{Fe}_{3-x}\text{GeTe}_2$, *Physical Review B* **96**, 144429 (2017).
- [44] H. Algaidi, C. Zhang, Y. Ma, C. Liu, A. Chen, D. Zheng, and X. Zhang, Magnetic critical behavior of van der waals Fe_3GaTe_2 with above-room-temperature ferromagnetism, *APL Materials* **12**, 10.1063/5.0183071 (2024).
- [45] Q. Liu, H. Zhang, and Y. Xu, Topology and magnetism interplay in layered van der waals magnets, *Adv. Mater.* **34**, 2105678 (2022).
- [46] Z. Liang, K. Hu, and W. Guo, Electronic structure engineering in MnBi_4Te_7 for spintronic devices, *Appl. Phys. Lett.* **122**, 112405 (2023).
- [47] J. Y. Law, V. Franco, L. M. Moreno-Ramírez, A. Conde, D. Y. Karpenkov, I. Radulov, K. P. Skokov, and O. Gutfleisch, A quantitative criterion for determining the order of magnetic phase transitions using the magnetocaloric effect, *Nature communications* **9**, 2680 (2018).
- [48] C. Triguero, M. Porta, and A. Planes, Magnetocaloric effect in metamagnetic systems, *Physical Review B—Condensed Matter and Materials Physics* **76**, 094415 (2007).
- [49] A. Arrott, Criterion for ferromagnetism from observations of magnetic isotherms, *Physical Review* **108**, 1394 (1957).
- [50] B. Banerjee, On a generalised approach to first and second order magnetic transitions, *Physics letters* **12**, 16 (1964).
- [51] A. Arrott and J. E. Noakes, Approximate equation of state for nickel near its critical temperature, *Physical Review Letters* **19**, 786 (1967).
- [52] A. Pramanik and A. Banerjee, Critical behavior at paramagnetic to ferromagnetic phase transition in $\text{Pr}_{0.5}\text{Sr}_{0.5}\text{MnO}_3$: A bulk magnetization study, *Physical Review B—Condensed Matter and Materials Physics* **79**, 214426 (2009).
- [53] K. A. Gschneidner, V. K. Pecharsky, and A. Tsokol, Recent developments in magnetocaloric materials, *Reports on progress in physics* **68**, 1479 (2005).
- [54] M.-H. Phan and S.-C. Yu, Review of the magnetocaloric effect in manganite materials, *Journal of Magnetism and Magnetic Materials* **308**, 325 (2007).